

# III

## Expansions-contractions Flows

### III.1 Introduction

Flows of viscoplastic materials through internal passages of abruptly varying cross sections are found in a wide variety of industrial and natural processes. A rather brief list of examples includes extrusion, mold filling, and flows through porous media. In such complex flows of viscoplastic materials, there are regions where the intensity of the stress tensor exceeds the yield stress. These regions are usually called yielded regions. The regions where the stress intensity falls below the material yield stress are called unyielded regions. Below the yield stress, a viscoplastic material behaves as a very high-viscosity liquid, and, at the yield stress, some kind of microstructure collapse occurs, causing the viscosity to fall dramatically [24]. The surfaces delimiting yielded and unyielded regions are called yield surfaces (e.g. [49]).

Some important issues related to complex flows of viscoplastic materials are still far from being well understood. One of them is concerned with the existence of yield surfaces when the Bingham equation is employed [50, 51, 52]. Another difficulty is related to the discontinuity of the Bingham equation, which renders it unsuitable to numerical computations of complex flows. To circumvent this problem, it is usual practice to employ some continuous version of the Bingham equation carrying a regularization parameter (e.g. [53, 54, 55]). The most commonly employed regularized equations are the ones proposed by Bercovier and Engelman [28], Papanastasiou [29], and, to a lesser extent, the bi-viscosity equation [56]. However, solutions obtained with regularized equations are invariably dependent on the value of the regularization parameter, especially regarding the determination of the yield surfaces [54].

Different flows of viscoplastic materials have been studied in the past. Al Khatib and Wilson [57] analyzed the development of Poiseuille flow of viscoplastic materials, using the bi-viscosity model. These same authors determined the yield surface in the orthogonal rheometer flow of a viscoplastic

material, using again the bi-viscosity equation [58]. Results were obtained both asymptotically and numerically, and they concluded that unyielded regions exist only for some combinations of the parameters.

Alexandrou et al. [59] studied numerically the flow of Herschel-Bulkley materials in a three-dimensional expansion. In their computations, they employed a Papanastasiou regularized equation modified to account shear thinning at high deformation rates. The ducts had square cross sections, and results were obtained for both the 2:1 and the 4:1 expansion rates. The effects of the Reynolds and Bingham numbers on the flow pattern and pressure distribution were investigated. A strong interplay between the effects of the Reynolds and Bingham numbers was observed to occur, influencing the formation and break up of unyielded zones in the corner of the expansion. Vradis and Ötügen [60] analyzed numerically the flow of Bingham materials through a  $1 \times 2$  axisymmetric abrupt expansion. They concluded that the reattachment length increases with the Reynolds number, decreases with yield number, and is essentially independent of the expansion ratio. Jay et al. [61] analyzed the flow of yield-stress materials through a 1:4 sudden axisymmetric expansion using bi-viscosity regularizations of the Herschel-Bulkley and Bingham equations. The influence of shear thinning, inertia and yield-stress values on the structure of the flow and on pressure and head losses was studied. They observed two toroidal unyielded regions, and concluded that inertia and yield stress act in opposite ways and that shear thinning reduces the dimensions of both vortices and dead zones.

The inertialess flow of Bingham materials past a sphere has been studied recently by Liu et al. [54]. Most of their numerical solutions were obtained with the aid of the regularized Bingham equation proposed by Bercovier and Engelman [28]. They showed that the location of the yield surfaces is a function of the regularization parameter such that the yielded regions increase in size as it is increased. Although they investigated fairly large values of the regularization parameter, no limiting behavior of the yield surface locations could be inferred.

In this chapter, the axisymmetric flow of viscoplastic materials through an abrupt expansion followed by an abrupt contraction is investigated. In the numerical solutions, the assumption of that the materials obey generalized Newtonian material constitutive model, with a viscosity function as proposed by de Souza Mendes and Dutra [24], is adopted. The parameters of this equation are all determined via least-squares fit to rheological data, and hence no regularization parameter is involved. Visualization experiments illustrate the dependence of the yield surface location on the rheological and flow

parameters.

## III.2 Analysis

### (a) Viscosity function and rheological parameters

The Carbopol dispersions present shear stress functions  $\tau(\dot{\gamma})$  that are well represented by the following equation [24]:

$$\tau = \left( 1 - \exp \left[ -\frac{\eta_o \dot{\gamma}}{\tau_o} \right] \right) (\tau_o + K \dot{\gamma}^n) \quad (1)$$

in this equation,  $\dot{\gamma}$  is the shear rate, while  $\eta_o$ ,  $\tau_o$ ,  $K$ , and  $n$ , are respectively the low shear rate viscosity, the yield stress, the consistency index, and the behavior or power-law index. The physical meaning of these material parameters is discussed in detail by de Souza Mendes and Dutra [24].

According to Eq. (1), when the stress  $\tau$  reaches the yield stress  $\tau_o$ , there is a sharp increase of the shear rate with no appreciable change in stress, i.e. the shear stress remains roughly equal to  $\tau_o$  while the shear rate value jumps from a value around  $\dot{\gamma}_o$  to an often much larger value in the vicinity of  $\dot{\gamma}_1$ , where

$$\dot{\gamma}_o \equiv \frac{\tau_o}{\eta_o}; \quad \dot{\gamma}_1 \equiv \left( \frac{\tau_o}{K} \right)^{1/n} \quad (2)$$

The jump number  $J$  proposed by de Souza Mendes [25] gives a relative measure of the shear rate jump that occurs at  $\tau = \tau_o$  [26]:

$$J \equiv \frac{\dot{\gamma}_1 - \dot{\gamma}_o}{\dot{\gamma}_o} = \frac{\eta_o \tau_o^{\frac{1-n}{n}}}{K^{1/n}} - 1 = \frac{\dot{\gamma}_1}{\dot{\gamma}_o} - 1 = \frac{1 - \dot{\gamma}_o^*}{\dot{\gamma}_o^*} \quad (3)$$

The jump number is thus a dimensionless rheological property of viscoplastic materials. When  $n = 1$ , it becomes independent of the yield stress  $\tau_o$  and reduces to  $J = \eta_o/K - 1$ , i.e. for  $n = 1$ ,  $J + 1$  becomes the ratio between  $\eta_o$  and the plastic viscosity.

Choosing  $\dot{\gamma}_1$  as characteristic shear rate and  $\tau_o$  as the characteristic stress, so that  $\tau^* \equiv \tau/\tau_o$  and  $\dot{\gamma}^* \equiv \dot{\gamma}/\dot{\gamma}_1$  are respectively the dimensionless versions of the shear stress and shear rate, then it is possible to write the following dimensionless form of Eq. (1) [27]:

$$\tau^* = (1 - \exp [-(J + 1)\dot{\gamma}^*]) (1 + \dot{\gamma}^{*n}) \quad (4)$$

And the dimensionless viscosity function is given by

$$\eta^* = \frac{\tau^*}{\dot{\gamma}^*} = \frac{\eta}{\eta_o}(J + 1) = (1 - \exp [-(J + 1)\dot{\gamma}^*]) \left( \frac{1}{\dot{\gamma}^*} + \dot{\gamma}^{*n-1} \right) \quad (5)$$

### (b) Governing equations and boundary conditions

The geometry considered is shown in Fig. III.1. The governing equations for this flow are made dimensionless by employing the following dimensionless variables:

$$\mathbf{v}^* = \frac{\mathbf{v}}{\dot{\gamma}_1 R}; \quad \mathbf{T}^* = \frac{\mathbf{T}}{\tau_o}; \quad p^* = \frac{p}{\tau_o}; \quad \nabla^* = R \nabla \quad (6)$$

where  $R$  is the small tube radius,  $\mathbf{v}$  is the velocity field,  $\mathbf{T}$  is the stress field, and  $p$  is the pressure field.

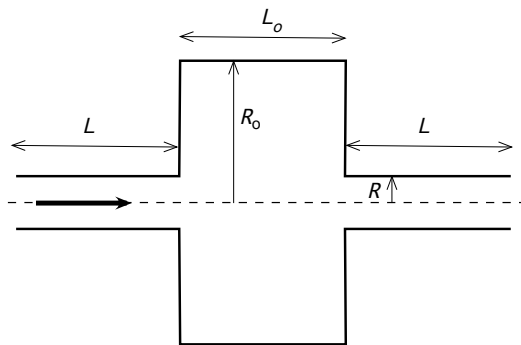


Figure III.1: The geometry.

The flow is isochoric, inertialess, laminar, steady, and axisymmetric. All the properties are considered to be temperature-independent, and viscous dissipation is assumed to be negligible. For this situation, the dimensionless mass and momentum conservation equations are:

$$\nabla^* \cdot \mathbf{v}^* = 0; \quad \nabla^* \cdot \mathbf{T}^* = \mathbf{0} \quad (7)$$

In this analysis it is assumed that the material behaves like the generalized Newtonian material model [6], given by:

$$\mathbf{T}^* = -p^* \mathbf{1} + \boldsymbol{\tau}^* = -p^* \mathbf{1} + \eta^*(\dot{\gamma}^*) \dot{\gamma}^* \quad (8)$$

where  $\boldsymbol{\tau}^*$  is the extra-stress tensor field,  $\dot{\gamma}^* = \nabla^* \mathbf{v}^* + (\nabla^* \mathbf{v}^*)^T$  is the rate-of-deformation tensor field,  $\dot{\gamma}^* \equiv \sqrt{\text{tr } \dot{\gamma}^{*2}}/2$  is a measure of its intensity, and  $\eta^*(\dot{\gamma}^*)$  is given by Eq. (5).

Defining  $\mathbf{n}$  and  $\mathbf{t}$  as unit vectors locally normal and tangent to a boundary surface, respectively, the boundary conditions are: no-slip and impermeability conditions at all solid boundaries ( $\mathbf{v}^* = \mathbf{0}$ ); symmetry condition at the centerline ( $\mathbf{n} \cdot (\nabla^* \mathbf{v}^*) \cdot \mathbf{t} = 0$  and  $\mathbf{v}^* \cdot \mathbf{n} = 0$ ); and fully developed flow at the outlet ( $\mathbf{n} \cdot \mathbf{T}^* = \mathbf{0}$ ). At the inlet, the axial velocity is assumed uniform ( $\mathbf{n} \cdot \mathbf{v}^* = \bar{u}^*$  and  $\mathbf{t} \cdot \mathbf{v}^* = 0$ ).

### (c) Governing parameters

The foregoing analysis indicates that this flow is governed by five dimensionless parameters. Two of these parameters are just rheological material properties, namely, the jump number,  $J$ , and the power-law exponent,  $n$ . There are also two geometrical parameters, namely, the diameter or radius ratio,  $R_o/R$ , and the length-to-radius ratio of the large tube,  $L_o/R_o$ . The last parameter is a flow parameter, and there are a number of equivalent choices for it. One possible choice is the dimensionless fully-developed wall shear stress at the upstream (or downstream) tube,  $\tau_R^*$ . Because the yield stress was taken as the characteristic stress, this parameter can also be seen as the reciprocal of a Bingham number. Another possible choice is the dimensionless average velocity of the material at the upstream (or downstream) tube,  $\bar{u}^*$ . It is clear that there is a one-to-one relationship between  $\bar{u}^*$  and  $\tau_R^*$ .

## III.3 Numerical Solution

The conservation equations of mass and momentum are discretized by the finite volume method described by Patankar [62] and solved with the aid of the FLUENT software. Staggered velocity components are employed to avoid

unrealistic pressure fields. The SIMPLE algorithm [62] is used, in order to handle the pressure / velocity coupling. The resulting algebraic system is solved by the TDMA line-by-line algorithm [62] with the block correction algorithm [63] to improve the convergence rate.

The length of the upstream and downstream small-diameter tubes was chosen to ensure the achievement of flow development both upstream the entrance of the large-diameter duct, and upstream the exit of the downstream tube ( $L/R = 10$ ).

To define the computational mesh, the domain was divided into five zones. Two zones (Zone 1 and Zone 2) correspond to the upstream and downstream tubes. The other three zones are in the central tube: the first (Zone 3) corresponds to the core region, up to a radius equal to the entrance tube radius (i.e., from  $r = 0$  to  $r = R$ ); the second one (Zone 4) is an intermediate zone that ranges from  $r = R$  to  $r = (R_o - R)/2$ ; and the last one (Zone 5) starts at  $r = (R_o - R)/2$  and ends at the central tube wall ( $r = R_o$ ). The mesh employed was uniform per zone in the axial and radial directions, with more refined meshes in the central tube zones.

Table III.1: Mesh test for  $\tau^* = 3.7$ ,  $J = 18000$  and  $n = 0.4$ .

Mesh	$N_1$	$N_2$	$N_3$	$N_4$	$N_5$	$\Delta p^*$	$\Phi$
1	60	30	38	68	68	1.448	0.23
2	80	40	50	90	90	1.637	0.265
3	100	50	65	110	110	1.626	0.246
4	120	60	75	135	135	1.506	0.214

To warrant mesh-independent solutions, extensive grid tests were performed. Four meshes were generated for the case with  $R_o/R = 6.3$  and  $L_o/R_o = 1$ . The mesh details are given in Table III.1, together with corresponding values of the head loss and displacement efficiency. The head loss is defined as

$$\Delta p^* = \frac{\Delta p}{4\tau_R} \quad (9)$$

where  $\Delta p$  is the difference between the pressure that would occur at any location in the fully-developed portion of the downstream small tube if there were no loss in the cavity and the actual pressure at the same location. The displacement efficiency is defined as

$$\Phi = \frac{V_{c,y}}{V_c} \quad (10)$$

where  $V_{c,y}$  is the volume of yielded liquid in the large-tube cavity, and  $V_c$  is the total volume of the cavity ( $V_c = \pi L_o(R_o^2 - R^2)$ ). The parameters  $N_i$  appearing in Tables III.1 and III.2 are the numbers of control volumes employed in different flow zones. More specifically, the meshes in Zones 1 and 2 (the upstream and downstream tubes) have both  $N_1$  control volumes in the axial direction and  $N_3$  control volumes in the radial direction. The three zones in the large-diameter tube have  $N_2$  control volumes in the axial direction; in the radial directions, Zone 3 has  $N_3$  control volumes, Zone 4 has  $N_4$  control volumes, and Zone 5 has  $N_5$  control volumes.

Table III.2: Meshes employed.

$R_0/R$	$L_0/R_0$	$N_1$	$N_2$	$N_3$	$N_4$	$N_5$
3.3	1	80	30	50	50	50
3.3	1.8	80	45	50	50	50
6.3	1	80	40	50	90	90
6.3	1.8	80	60	50	90	90
10	1	80	40	30	100	110
10	1.8	80	40	60	100	110

It can be observed in Table III.1 that the differences between the results obtained with the three finest meshes are very low. Velocity profiles in the center of the cavity ( $x = L + L_0/2$ ) and the mean pressure profiles were also compared, and no difference was observed. Therefore, the mesh with 200 control volumes in the axial direction, and 230 in the radial direction was chosen. For the other geometries, the meshes were chosen using the same procedure. Details of the meshes used for the other cases are given in Table III.2.

## III.4 The Experiments

### (a) The visualization experiments

Fig. III.2 depicts the flow visualization apparatus. The materials employed in the visualization experiments are Carbopol aqueous dispersions containing micron-size spheres to promote light reflection. The test section was built in transparent plexiglas, and consists of two identical small-diameter tubes attached, one at each end, to a larger-diameter tube. The couplings

are made with the aid of two plexiglas disks previously machined to provide the appropriate fitting and sealing. The inner diameter of the small tubes is  $2R = 8$  mm, and their length is  $L = 20$  mm. Different lengths  $L_o$  and diameters  $2R_o$  of the large-diameter tube were employed, to allow the study of the effects of the ratios  $R_o/R$  and  $L_o/R_o$  within a representative range.

The other main components of the test rig are a tank, a metering pump, and a glass box. The pump sucks the Carbopol dispersion from the tank and pushes it into the test section. After leaving the test section, the material flows back into the tank. The tank is large enough (about 4 L) and the flow rates are low enough (of the order of one liter per hour) to ensure that the material traverses the flow circuit only once. A laser sheet is employed to produce a sheet of light containing the channel axis. After the steady state is attained for a given flow rate, a CCD camera records the particle paths. During the visualization tests, the glass box that surrounds the tube is kept full with glycerol, to help eliminating image distortion due to refraction.

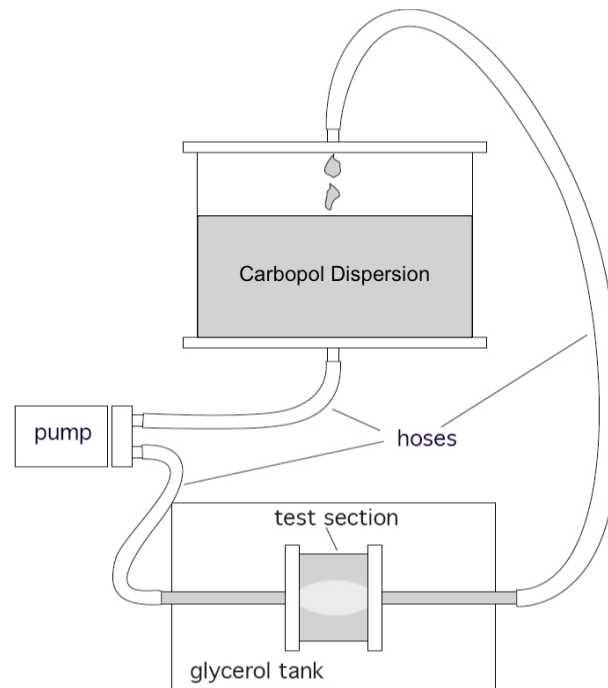


Figure III.2: Schematics of the apparatus.

The yield surface is made visible by choosing large enough exposure times that allow sufficient particle displacement in the yielded region. Thus, while the particle paths in the yielded region are recorded as white lines, the stagnant particles in the unyielded region appear as white dots in the pictures. Because of the sharp velocity change across the yield surface, its location appears

quite clearly. In many of the pictures obtained, a mild increase in particle concentration seems to occur near the yield surface, probably due to shear-induced dispersion, facilitating further the visualization of the yield surface location.

The shear stress at the wall of the small tubes,  $\tau_R$ , appearing in the flow parameter  $\tau_R^* = \tau_R/\tau_o$  was evaluated by obtaining, for each flow rate, the numerical solution of the momentum equation for the fully developed flow through the upstream or downstream tube.

### (b) Rheology of the Carbopol dispersions

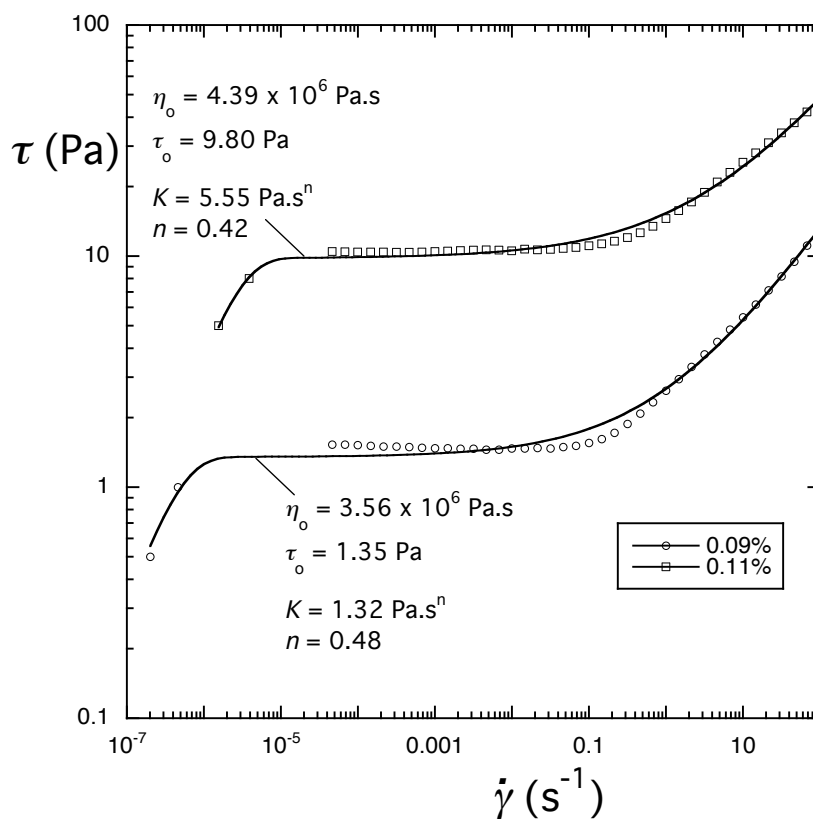


Figure III.3: The flow curves of the Carbopol dispersions.

Aqueous dispersions of Carbopol 676 at different concentrations were employed in the flow experiments. The dispersions were NaOH-neutralized to achieve a pH of about 7. The viscosity function of these materials was obtained with an ARES rotational rheometer at controlled strain mode and a modified Couette geometry designed to circumvent possible apparent-slip problems (e.g. [21, 22]). The modification consists of the introduction of longitudinal grooves on both the bob and the cup surfaces. The grooves are 1-mm deep, 2-mm wide, and roughly 2-mm spaced. This geometry was successfully tested with standard

Newtonian mineral oils. The results obtained essentially coincided with the corresponding ones obtained with smooth surfaces. Each data point was taken only after achievement of steady state. The data-points corresponding to the lowest shear rate were obtained from creep experiments performed in a UDS 200 Paar-Phisica rheometer, because the rate-sweep tests of the ARES rheometer employed could not handle such low shear rates. In these creep tests, a constant stress below the yield stress is imposed, and, once steady flow is attained, typically after up to 48 hours, the corresponding shear rate is obtained. Flow curves were obtained both with fresh samples and with samples collected after the experiments, and no significant degradation signs were observed.

The results obtained are shown in Fig. III.3. The curve fittings employing Eq. (1) are shown to reproduce well the data obtained. It is seen that the Carbopol dispersions present a highly viscoplastic behavior, characterized by the sharp viscosity change at the yield stress. In Fig. III.4, the dimensionless viscosity is plotted as a function of the dimensionless shear stress.

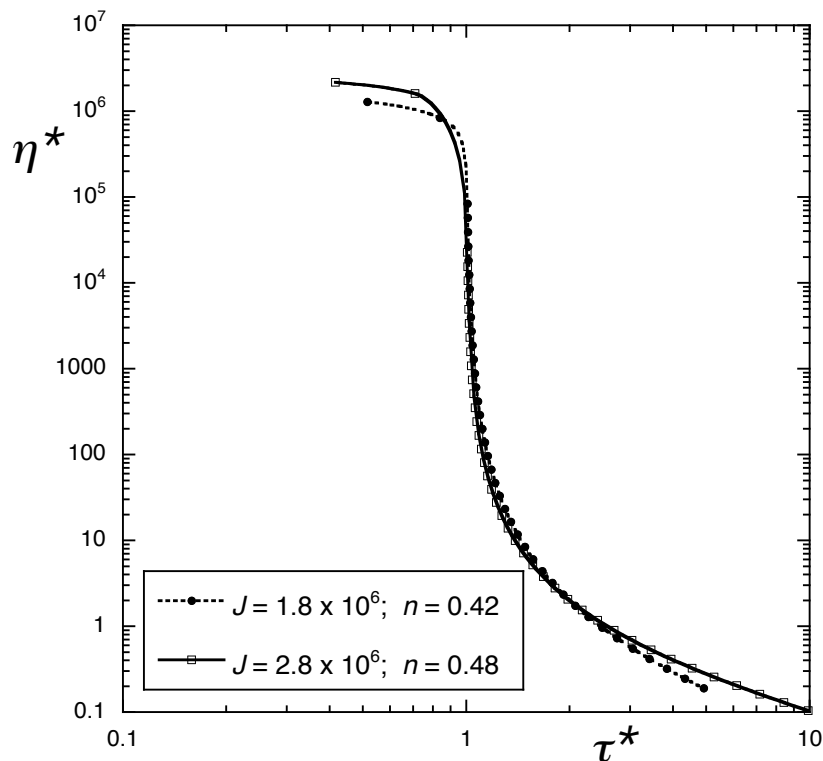


Figure III.4: The dimensionless viscosity of the Carbopol dispersions as a function of the dimensionless shear stress.

## III.5 Results and Discussion

### (a) Flow visualization results

In all the pictures of this section only the flow in the large tube is shown, and the flow direction is from left to right. The Reynolds number based on the small tube diameter is always kept below 0.1, to ensure negligible inertia.

The yielded region is seen to have a peculiar apple-like shape. At the large tube inlet, the yield surface intersects the expansion plane at some radial distance from the rim. In the region close to the large tube exit, the yield surface presents a milder curvature, and intersects the contraction plane close to the exit rim.

Due to space limitations, only a few photo sequences are now presented to illustrate the main trends observed experimentally for a wider range of parameters. Fig. III.5 shows the dependence of the yield surface location on  $\tau_R^*$ . It is clear from this figure that the size of the yielded region increases as  $\tau_R^*$  is increased, as expected, because as  $\tau_R^*$  is increased the stress level in the large tube increases, attaining values above unity in a larger portion of this region. The last picture on the right of Fig. III.5 was taken at zero flow rate after the highest flow rate experiment is finished. A mild concentration of the spherical particles at the yield surface can be observed in this picture, probably due to shear-induced dispersion.

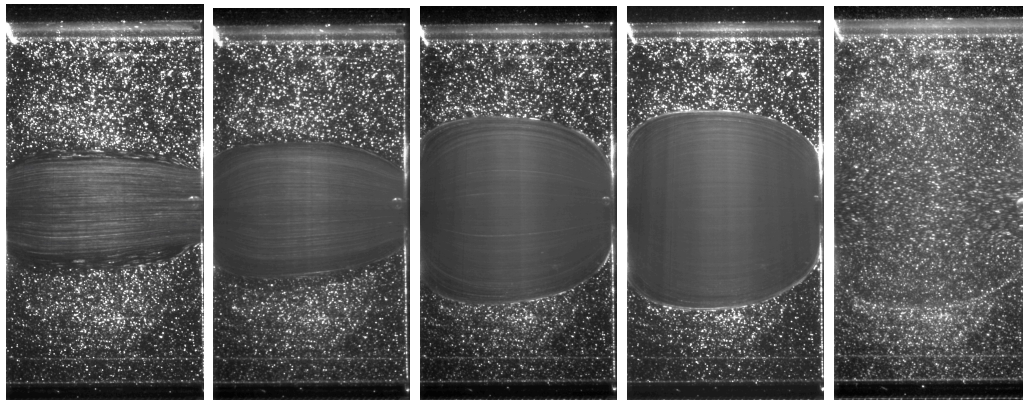


Figure III.5: Effect of  $\tau_R^*$  on the yield surface location, for  $J = 2.8 \times 10^6$ ,  $n = 4.8$  (Carbopol 0.09%),  $L_o/R_o = 1.0$ , and  $R_o/R = 5$ . From left to right, the pictures correspond respectively to  $\tau_R^* = 3.0, 5.3, 8.4, 10.5$ , and 0.0.

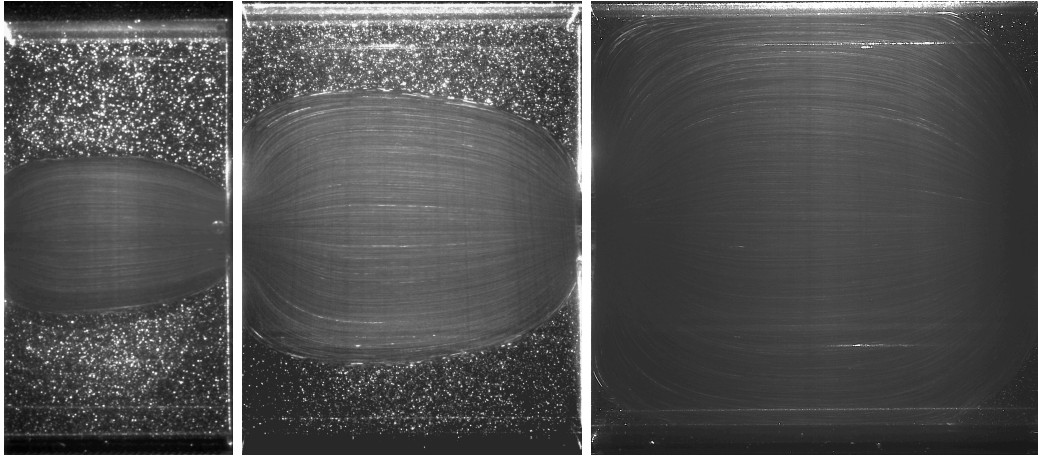


Figure III.6: Effect of  $L_o/R_o$  on the yield surface location, for  $J = 2.8 \times 10^6$ ,  $n = 4.8$  (Carbopol 0.09%),  $\tau_R^* = 5.3$ , and  $R_o/R = 5$ . From left to right, the pictures correspond respectively to  $L_o/R_o = 1.0, 1.5$ , and  $2.0$ .

Concerning  $L_o/R_o$ , Fig. III.6 shows that the size of the yielded region increases as this geometrical parameter is increased. Thus, the displacement efficiency decreases as the depth of the cavity is increased, as expected.

The influence of the radius ratio  $R_o/R$  on the yield surface location can be observed in Fig. III.7. In this figure it is observed that the yielded region decreases significantly as  $R_o/R$  is increased.

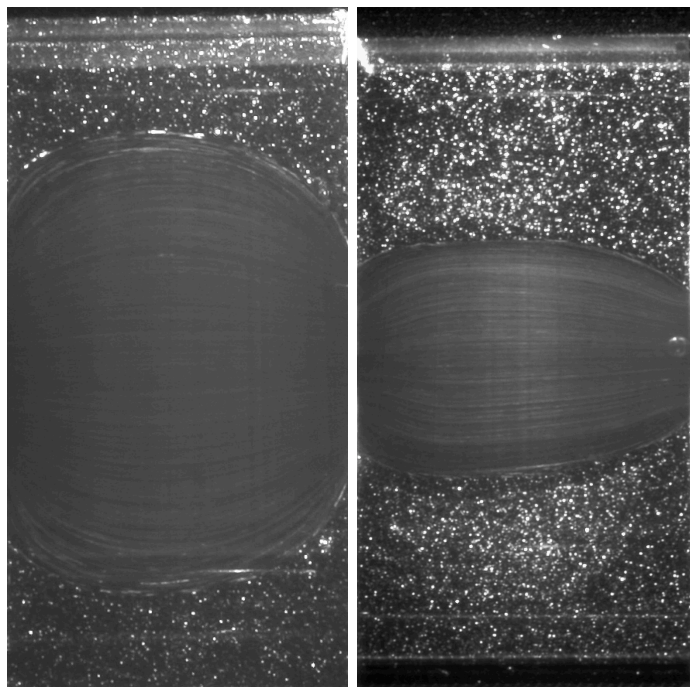


Figure III.7: Effect of  $R_o/R$  on the yield surface location, for  $J = 2.8 \times 10^6$ ,  $n = 4.8$  (Carbopol 0.09%),  $\tau_R^* = 5.3$ , and  $L_o/R_o = 1.0$ . From left to right, the pictures correspond respectively to  $R_o/R = 3$  and  $5$ .

Fig. III.8 illustrates the effect of the material rheology on the location of the yield surface. It is clear from these figures that the size of the yielded region is larger for the more concentrated dispersion. It is not clear whether this trend is due to the change in  $J$  or in  $n$ , and a definitive assessment would only be possible with additional data for other concentrations. However, it seems more likely that it is the increase in the power-law index  $n$  that is responsible for the reduction in size of the yielded region, due to the following reasons. Firstly, the jump number values for the two concentrations are rather close to each other (Fig. III.4), while the numerical studies to be presented below (Fig. III.16) indicate that the yielded region size increases quite mildly with  $J$ . Secondly, these same studies show that it decreases with  $n$  (Fig. III.17) as observed in Fig. III.8.

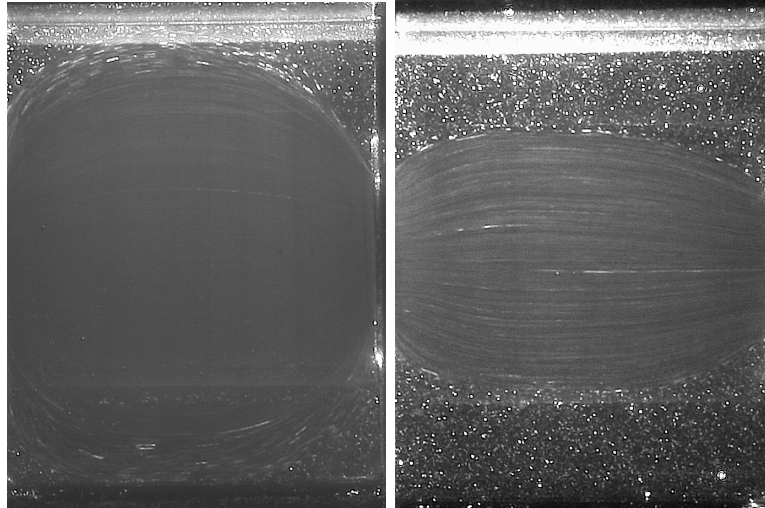


Figure III.8: Effect of rheology on the yield surface location, for  $\tau_R^* = 4.0$ ,  $R_o/R = 3$ , and  $L_o/R_o = 1.5$ . From left to right, the pictures correspond respectively to  $(J, n) = (1.8 \times 10^6, 0.42)$  and  $(2.8 \times 10^6, 0.48)$ .

The experimental observations of the size of the yielded region are summarized in Figs. III.9 and III.10. The displacement efficiencies shown in these figures have been estimated from the photographs. The trends observed in these figures have already been discussed above.

Finally for this section, it is important to mention an interesting instability that was sometimes observed, especially at lower flow rates, just before the establishment of steady state. More specifically, a typical experiment starts by turning on the pump at a fixed flow rate. In the cases where the instability was observed, a pseudo-steady state was firstly attained with a given yielded region size. After a few minutes, however, the yielded region undergoes a

significant and abrupt reduction to its final steady-state size.

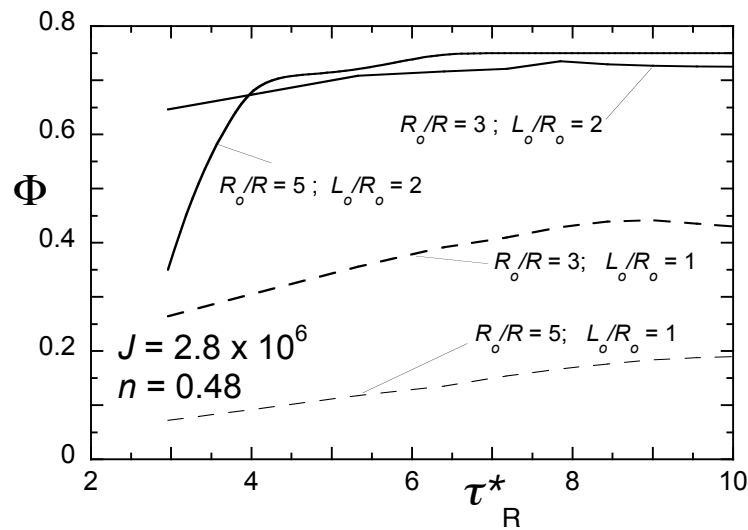


Figure III.9: Displacement efficiency as a function of  $\tau_R^*$ . Carbopol 0.09%.

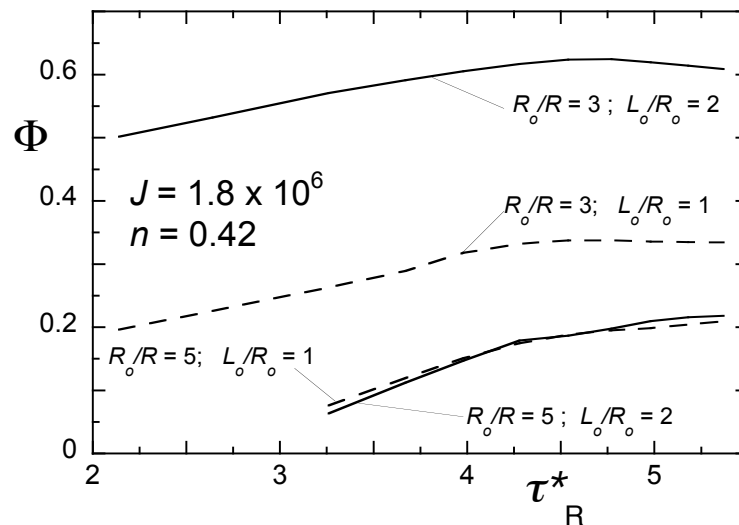


Figure III.10: Displacement efficiency as a function of  $\tau_R^*$ . Carbopol 0.11%.

## (b) Numerical results

The results presented in this section pertain to jump number values below the ones measured for the Carbopol dispersions, due to convergence problems experienced for high values of  $J$ .

Figs. III.11 and III.12 illustrate the distribution of the intensity of the dimensionless extra-stress field  $\tau^* = \sqrt{tr \tau^{*2}/2}$  for two different values of

$\tau_R^*$ , namely, 1.9 and 3.6, respectively. As expected, these figures show that the highest stress levels are found at the walls of the small tubes and in the vicinity of the rims. In the large tube, the stress decreases toward the wall.

The isoband corresponding to  $\tau^* = 1$ , within which is situated the yield surface, intersects the expansion and contraction planes at some radial distance from the rims, and, as  $\tau_R^*$  is increased, this isoband is pushed into the large-tube cavity. A small closed unyielded region is found in the axis and at mid-length of the large tube (Fig. III.12). This unyielded region occurs due to the transition, along the large-tube axis, from expansion flow (bi-axial extension) to contraction flow (uni-axial extension).

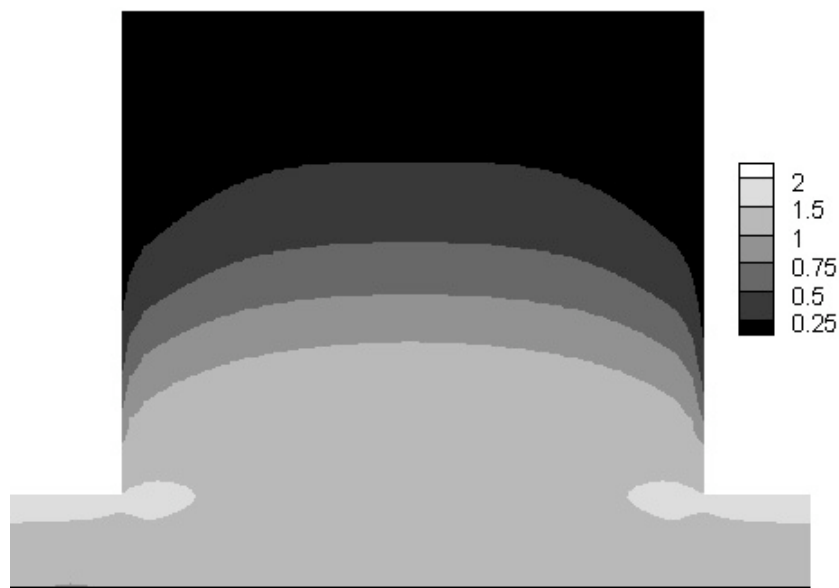


Figure III.11: Isobands of  $\tau^*$ .  $R_o/R = 6.3$ ,  $L_o/R_o = 1$ ,  $J = 18000$ ,  $n = 0.4$ ,  $\tau_R^* = 1.9$

Plug-flow regions are expected around the axis in the fully-developed regions of the flow in the small tubes. These are not shown in Figs. III.11 and III.12. In the short lengths of the upstream and downstream small tubes shown, the flow is under the influence of the presence of the large tube.

The stress fields shown in Figs. III.11 and III.12 are symmetric with respect to a mid-plane orthogonal to the axis, consistently with the equations of motion that originated them, which neglect inertia and assume a purely viscous material. This symmetry is not observed in the visualization experiments, as discussed earlier. This qualitative difference between the numerical results and the flow visualization results are attributed to the elastic behavior

of the Carbopol dispersions at stress levels below the yield stress.



Figure III.12: Isobands of  $\tau^*$ .  $R_o/R = 6.3$ ,  $L_o/R_o = 1$ ,  $J = 18000$ ,  $n = 0.4$ ,  $\tau_R^* = 3.6$

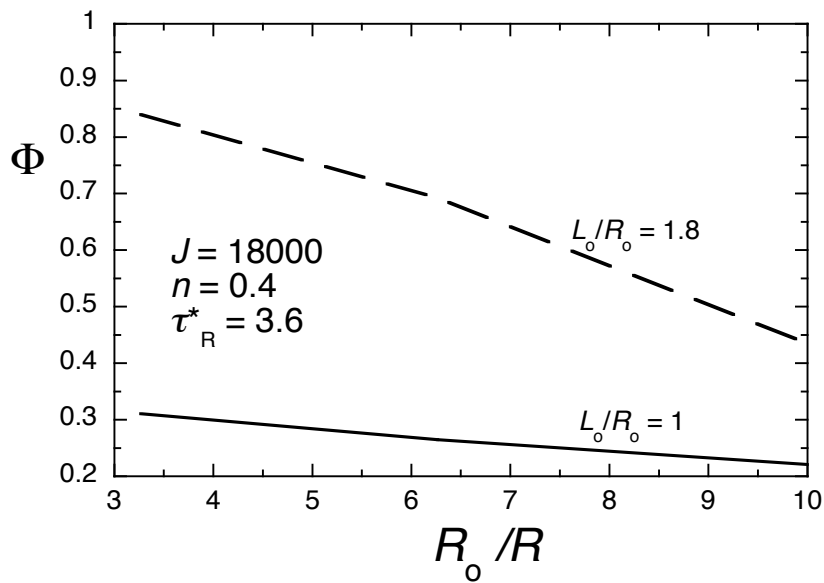


Figure III.13: Displacement efficiency as a function of  $R_o/R$ .  $\tau_R^* = 3.6$ ,  $J = 18000$ ,  $n = 0.4$ .

In order to assess the effects of the various parameters, there are presented the numerical results in terms of two global quantities, namely, the

displacement efficiency,  $\Phi$ , and the head loss,  $\Delta p^*$ . Both quantities are defined in Sec. ??.

In Fig. III.13 it is possible to see that the displacement efficiency is a decreasing function of the radius ratio  $R_o/R$ , because larger values of  $R_o/R$  imply deeper cavities, where the yielded region tends to occupy a relatively smaller volume. For very large values of  $R_o/R$ , the size of the yielded region should become insensitive to this parameter, and  $\Phi$  is expected to approach zero asymptotically. However, this range of  $R_o/R$  was not investigated here.

In Fig. III.14 it is seen that the displacement efficiency increases as  $L_o/R_o$  is increased, because larger values of  $L_o/R_o$  imply shallower cavities, where the yielded region tends to occupy a relatively larger volume.

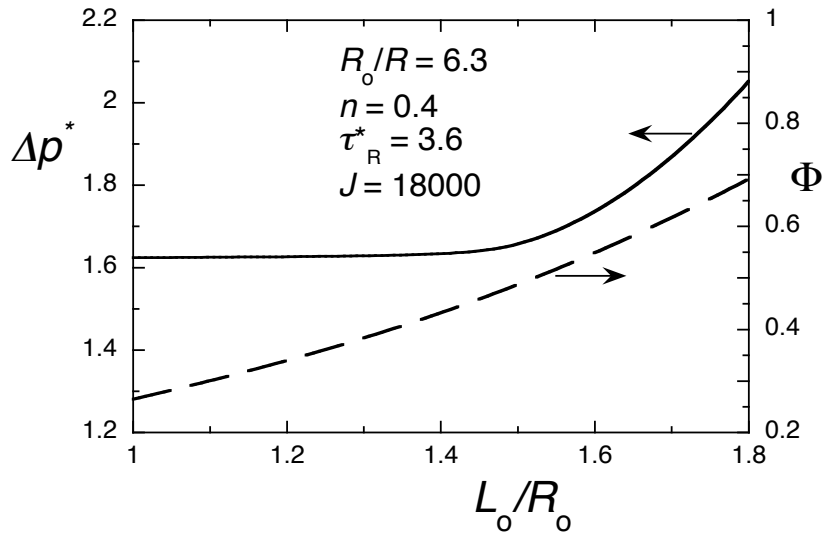


Figure III.14: Head loss and displacement efficiency as a function of  $L_o/R_o$ .  $\tau_R^* = 3.6$ ,  $R_o/R = 6.3$ ,  $n = 0.4$ ,  $J = 18000$ .

The displacement efficiency increases as the flow parameter  $\tau_R^*$  is increased, as illustrated in Fig. III.15. This trend is also in agreement with the flow visualization results. Fig. III.16 illustrates the dependency of the displacement efficiency on the jump number. It is observed that  $\Phi$  increases as  $J$  is increased, as also observed in the visualization experiments. This trend is in agreement with the results of Liu et al. [54] in their study of the effect of the regularization parameter on the yielded region size. The dependency of  $\Phi$  on the power-law exponent is illustrated in Fig. III.17. As  $n$  is increased,  $\Phi$  decreases, indicating that shear-thinning viscoplastic materials are displaced more easily than Bingham-like viscoplastic materials, because shear thinning

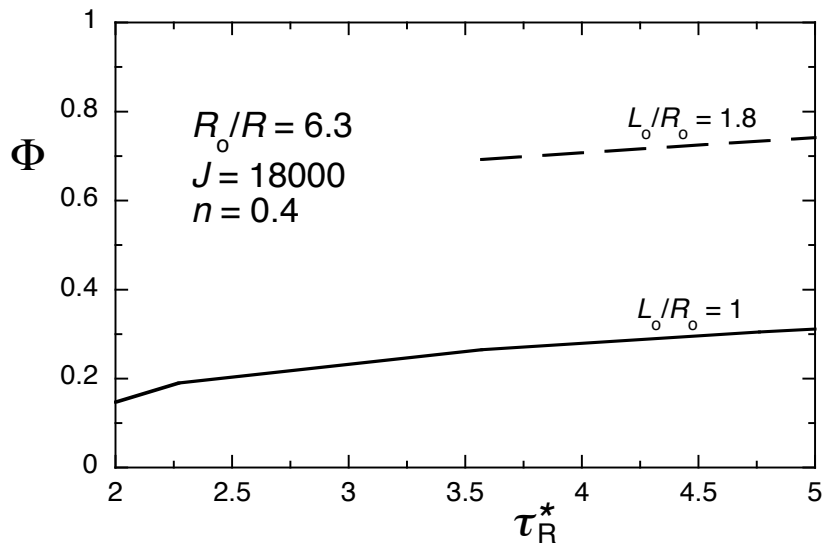


Figure III.15: Displacement efficiency as a function of  $\tau_R^*$ .  $R_o/R = 6.3$ ,  $J = 18000$ ,  $n = 0.4$ .

tends to cause larger deformation rates and hence larger yielded regions.

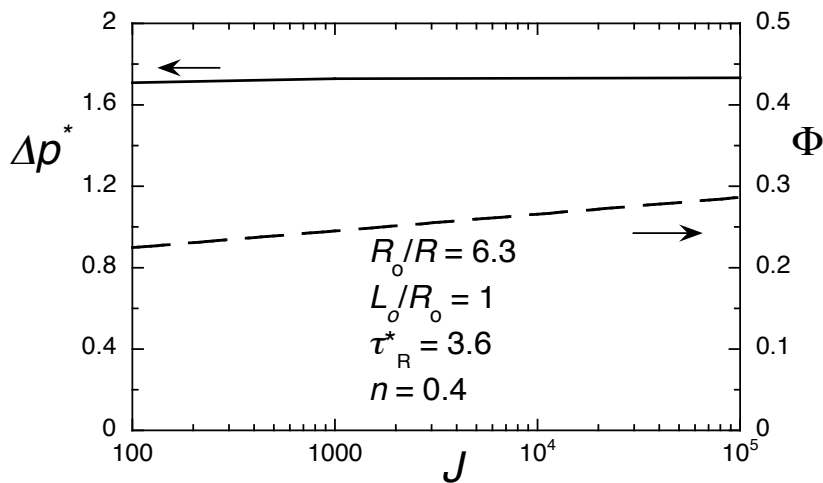


Figure III.16: Head loss and displacement efficiency as a function of the jump number.  $\tau_R^* = 3.6$ ,  $R_o/R = 6.3$ ,  $n = 0.4$ ,  $J = 18000$ .

Now, the results pertaining to the head loss  $\Delta p^*$ , shown in Figs. III.14-III.19 are examined. In Fig. III.14 it is seen that  $\Delta p^*$  is quite insensitive to  $L_o/R_o$  in the range  $1 < L_o/R_o < 1.5$ , but as this parameter is further increased the head loss increases considerably. Regarding the dependency on the radius ratio  $R_o/R$ , Fig. III.18 illustrates that the head loss increases as the cavity depth is increased, and for each set of values of the other parameters

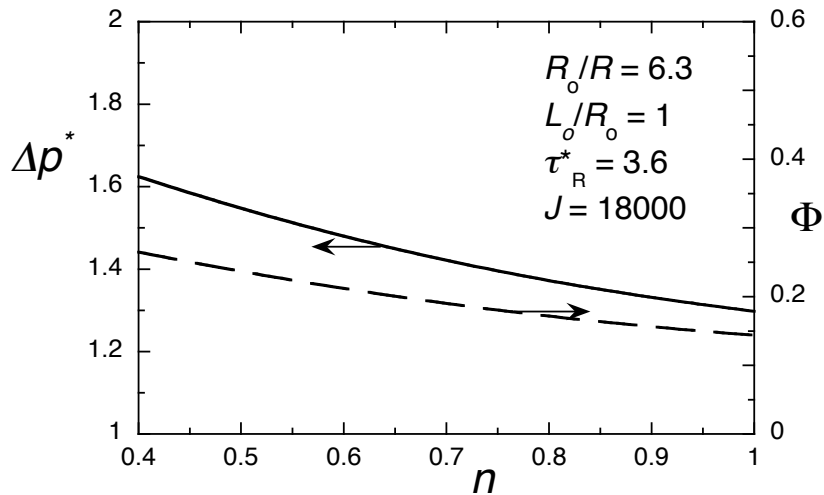


Figure III.17: Head loss and displacement efficiency as a function of the power-law index.  $\tau_R^* = 3.6$ ,  $R_o/R = 6.3$ ,  $L_o/R_o = 1$ ,  $J = 18000$ .

it is expected to reach an asymptotic value at sufficiently large values of  $R_o/R$ .

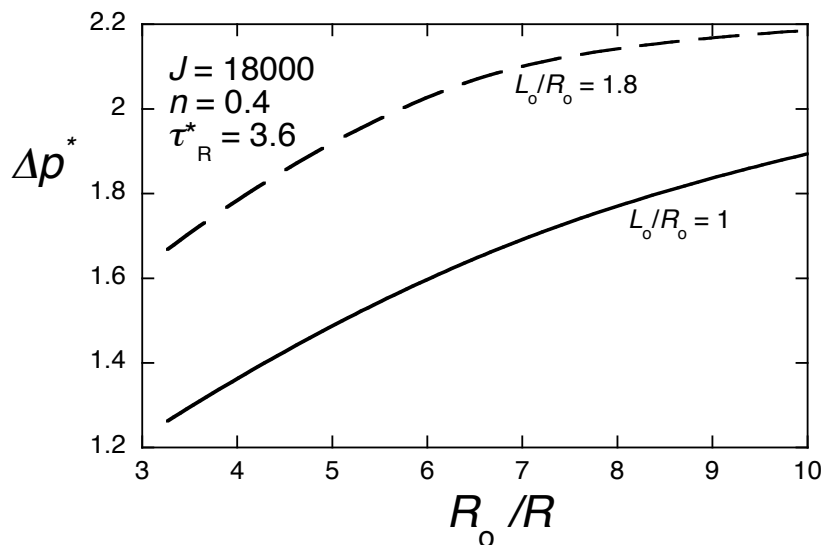


Figure III.18: Head loss as a function of  $R_o/R$ .  $\tau_R^* = 3.6$ ,  $J = 18000$ ,  $n = 0.4$ .

Fig. III.19 shows that  $\Delta p^*$  decreases as the flow parameter  $\tau^*$  is increased, indicating that the dimensional head loss in the large tube increases more slowly with  $\tau^*$  than the dimensional wall shear stress at the small tubes. This is because the relative contribution of the large tube to the total head loss decreases as the flow rate is increased. Regarding the rheological parameters,  $\Delta p^*$  is quite insensitive to the jump number (Fig. III.16), while it decreases as the power-law exponent  $n$  is increased (Fig. III.17), because larger values of  $n$

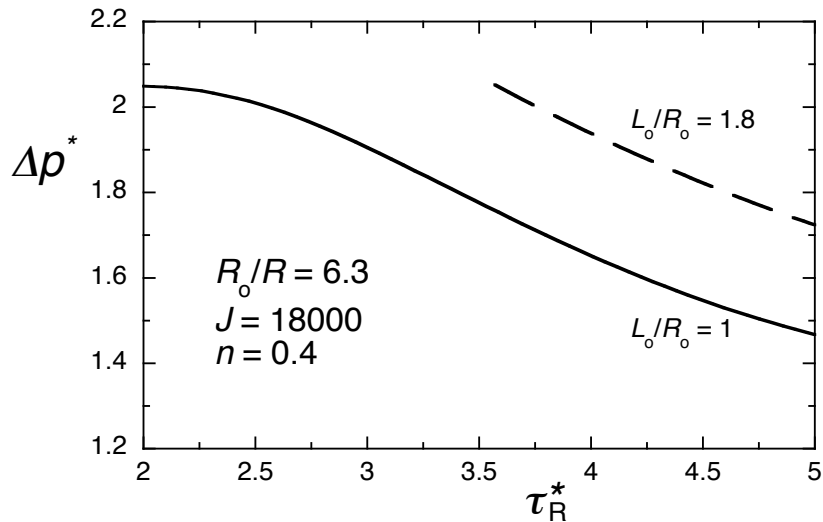


Figure III.19: Head loss as a function of  $\tau_R^*$ .  $R_o/R = 6.3$ ,  $J = 18000$ ,  $n = 0.4$ .

imply higher viscosities, causing the relative contribution of the large tube to the total head loss to decrease.

### (c) Comparison between experimental and numerical results

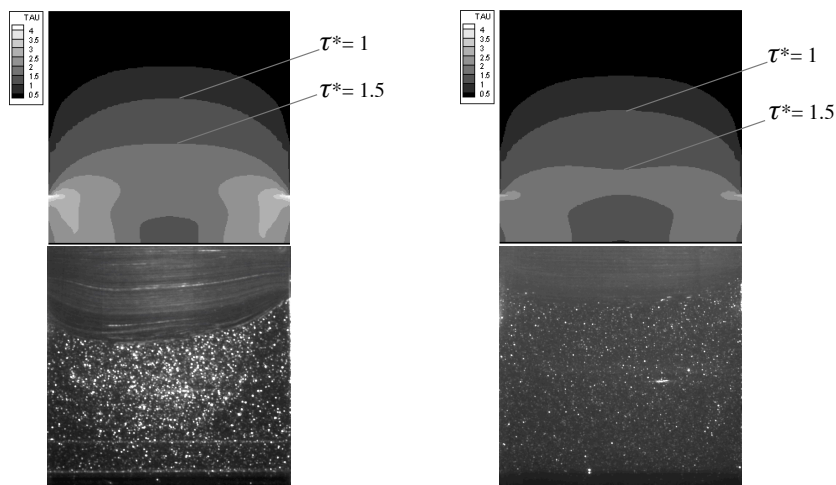


Figure III.20: Comparison between the predicted and observed yield surface locations.  $R_o/R = 5$ , and  $L_o/R_o = 1$ . Left: Carbopol 0.09% and  $\tau_R^* = 4.0$ ; right: Carbopol 0.11% and  $\tau_R^* = 2.6$ .

Fig. III.20 shows a comparison between the yield surface locations predicted and observed experimentally, for two sets of the governing parameters. At the bottom, the picture on the right pertains to Carbopol 0.09% ( $J = 2.8 \times 10^6$ ,  $n = 0.48$ ), whereas the one on the left is for Carbopol 0.11% ( $J = 1.8 \times 10^6$ ,  $n = 0.42$ ). At the top, the corresponding isobands

of stress intensity are given. These isobands were both obtained numerically for  $J = 4.0 \times 10^5$ , the highest jump number value for which convergence was achieved. These numerical results do not differ from the ones obtained for  $J = 1.0 \times 10^5$ , which indicates that the results shown are also representative of the jump number values of the experiments.

In the numerical results, the isoband corresponding to  $\tau^* = 1$ , within which is situated the yield surface, delimits much larger yielded regions than the corresponding ones observed experimentally, especially for the 0.11% concentration.

Fig. III.21 gives the numerically obtained radial distributions of the axial velocity and stress intensity at the symmetry plane, for the same case of the isobands shown on the top left of Fig. III.20. This figure shows that for Carbopol 0.09% the predicted yield surface ( $\tau^* = 1$ ) intersects the symmetry plane at the radial position  $r^* \equiv r/R \simeq 3$ , while non-negligible ( $u^* > 0.05$ ) axial velocity values are only found where  $r^* < 2$ , or where  $\tau^* > 1.5$ . Thus, if we chose  $\tau^* = 1.5$  (rather than  $\tau^* = 1$ ) to define the yield surface, then the numerical predictions and experimental results in Fig. III.20 would be in reasonable agreement for this case, because the experimentally observed yield surface intersects the symmetry plane at  $r^* \simeq 2$ .

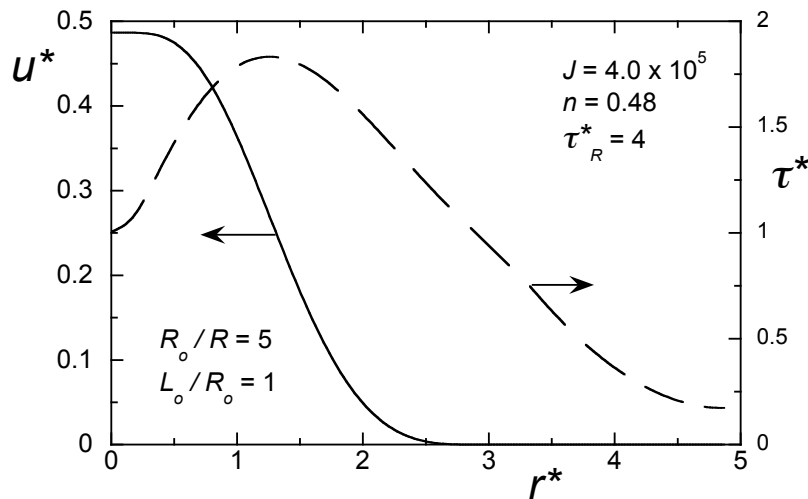


Figure III.21: Predicted axial velocity and stress intensity radial distributions at the symmetry plane.  $R_o/R = 5$ ,  $L_o/R_o = 1$ , and  $\tau_R^* = 4.0$ .  $J = 4.0 \times 10^5$  and  $n = 0.48$ .

## III.6 Final Remarks

In this chapter, the flow of viscoplastic materials through axisymmetric internal passages composed by an abrupt expansion followed by an abrupt contraction was studied. Numerical solutions of the mass and (inertialess) momentum conservation equations were obtained, in conjunction with the generalized Newtonian material constitutive model and a viscosity function proposed by de Souza Mendes and Dutra [24]. Visualization experiments with aqueous Carbopol dispersions at different concentrations were also performed.

The scaling of the equations of motion showed that this flow is governed by five dimensionless parameters, two of these being just rheological material properties, namely, the jump number,  $J$ , and the power-law exponent,  $n$ . Two other are geometrical parameters, namely, the diameter or radius ratio,  $R_o/R$ , and the length-to-radius ratio of the large tube,  $L_o/R_o$ . The last parameter is a flow parameter, chosen to be the dimensionless fully-developed wall shear stress at the upstream (or downstream) tube,  $\tau_R^*$ .

The displacement efficiency (volume of yielded material in the large-tube cavity / total volume of the cavity) is observed to increase with  $\tau_R^*$ . Regarding rheological parameters, the displacement efficiency increases mildly with the jump number and decreases as the power-law exponent is increased. The dependence with the geometrical parameters is such that the displacement efficiency decreases with  $R_o/R$  and increases with  $L_o/R_o$ . A comparison between experimental observations and numerical predictions suggests that the stress intensity on the yield surface is actually higher than the yield stress ( $\tau^* \simeq 1.5$ ), because at stresses below this value the viscosity value is still too high (Fig. III.4), and hence the velocity remains negligibly low.

## III.7 Note

In this chapter it was realized an analysis of expansions-contractions flows. Sec. III.1 is a bibliography review about the subject performed by prof. de Souza Mendes. In Sec. III.2 the governing equations found in the bibliography review are shown. Sec. III.3 deals with the numerical solution of expansions-contractions flows performed by profs. Naccache and de Souza Mendes. In Sec. III.4 the experiments realized by myself in partnership with Priscilla Vargas are described. The results of this research are shown and discussed in Sec. III.5, and some final remarks can be found in Sec. III.6. This research in which I collaborated was led by prof. de Souza Mendes.